Kobe University Repository : Kernel

PDF issue: 2026-11-08

Single-Nanometer-Sized Boron and Phosphorus Co-Doped Silicon Nanoparticles for Negative Electrode of Lithium-Ion Batteries

Yoshikawa, Hiroki ; Ueshima, Taiki ; Sugimoto, Hiroshi ; Xu, Jingchao ; Mizuhata, Minoru ; Fujii, Minoru

(Citation)
ACS Applied Nano Materials,7(24):27830-27836

(Issue Date)
2024-12-27

(Resource Type)
journal article

(Version)
Accepted Manuscript

(Rights)
This document is the Accepted Manuscript version of a Published Work that appeared in final form in Journal Title, copyright © American Chemical Society after peer review and technical editing by the publisher. To access the final edited and published work see https://doi.org/10.1021/acsanm.3c04824

(URL)
https://hdl.handle.net/20.500.14094/0100488650

KOBE UNIVERSITY

Single-Nanometer-Size Boron and Phosphorus Co-Doped Silicon Nanoparticles for Negative Electrode of Lithium-Ion Batteries

Hiroki Yoshikawa,[†] Taiki Ueshima,[†] Hiroshi Sugimoto,[†] Jingchao Xu,[‡] Minoru Mizuhata,[‡] and Minoru Fujii[†]*

[†]Department of Electrical and Electronic Engineering, Graduate School of Engineering, Kobe University, Rokkodai, Nada, Kobe 657-8501, Japan

*e-mail: fujii@eedept.kobe-u.ac.jp

[‡]Department of Chemical Science and Engineering, Graduate School of Engineering, Kobe University, Rokkodai, Nada, Kobe 657-8501, Japan

ABSTRACT

A Si-based negative electrode for lithium ion batteries (LIBs) is produced from methanol solutions of single-nanometer-size B and P co-doped Si nanoparticles (NPs) by drop-coating the solution on a substrate in air without using binders and conductive additives. Stable charge-discharge cycles are observed for films produced from Si NPs in the size range from less than 2 nm to 12.5 nm in diameter. It is shown that the performance and the stability of the electrodes depend strongly on

the size. The initial capacity increases with the size, while the stability decreases. The optimum diameter is ~7 nm. In the electrode made from 7 nm-diameter B and P co-doped Si NPs, the capacity is ~3300 mAh/g and the coulombic efficiency is ~97 % at a charge-discharge rate of 0.2C-rate.

Keywords: Silicon, Nanoparticle, Single-nanometer size, Doping, Boron, Phosphorous

1. INTRODUCTION

Lithium-ion batteries (LIBs) have commonly been used in portable electronic devices, power tools, electric vehicles (EVs), and energy storage systems.[1–5] To deal with the everlasting requirement to increase the energy density, silicon (Si)-based materials are gaining attention as a new negative electrode material due to their significantly higher theoretical capacity compared to graphite-based materials[6–8] and safety.[9,10] Disadvantages of Si-based electrodes are the small electrical conductivity, the formation of unstable solid electrolyte interphase (SEI), and the significant volume expansion (300-400 %) during charge-discharge cycles. The volume expansion leads to the structural breakdown, and cracks formed on SEI expose fresh Si surface and cause the formation of new SEI. This reduces the battery capacity due to continuous consumption of Li and electrolyte.[11–13]

An effective approach to address the stability problem of a Si-based electrode is incorporating structural buffer in an electrode, i.e., nanostructuring of an electrode, to absorb the volume expansion.[14–22] A variety of Si nanostructures have been tested and the structural damage is shown to be alleviated when the size of the nanostructures is smaller than ~150 nm.[23] For example, in an electrode with a core-shell fibrous structure composed of Si nanoparticles (NPs) tens of

nanometers and carbon nanotubes, an initial discharge capacity of 1305 mAh/g and 99 % capacity retention after 100 cycles at 0.2C-rate are achieved.[24] In an electrode with Si NPs 10 nm in diameter coated with carbon, an initial discharge capacity of 3380 mAh/g and 98 % capacity retention after 40 cycles are reported.[25] These results raise an expectation that higher performance and stability might be achieved by further reducing the size of Si NPs. However, experimental studies on a negative electrode made from Si NPs smaller than 10 nm in size are very limited due to the structural instability such as the low oxidation resistance.

In addition to the nanostructuring, alloying with other elements such as boron (B),[26–28] phosphorus (P),[29–33] nitrogen (N),[34] carbon (C),[35] and germanium (Ge)[36,37] improves the stability of a Si-based electrode. For example, an increase in structural stability during the charge-discharge cycle is reported in heavily P doped Si NPs 100-500 nm in size.[29] Similarly, in an eggshell-structured N-doped Si composite, an improvement in the stability of the interface between an electrode and electrolyte is reported.[34]

In this work, we apply the alloying strategy to single-nanometer-size Si NPs to improve the stability for charge-discharge cycles. We have developed spherical Si NPs smaller than 10 nm in diameter in which B and P are heavily doped.[38–40] In B and P codoped Si NPs, the energy levels are modified by the impurity doping as well as the quantum size effects, and the photoluminescence energies are a few hundred meV lower than those of undoped Si NPs with comparable sizes.[41] The co-doping modifies not only the energy level structures of Si NPs, but also the chemical properties. For example, the B and P co-doped Si NPs have the negative surface potential and are dispersible in aqueous media without any surface functionalization processes. Furthermore, they have high oxidation resistance compared to undoped Si NPs with comparable sizes, and exhibit superior performance as a photocatalyst and a photoelectrode for hydrogen

evolution.[42,43] These properties arise from the specific core/shell structure of co-doped Si NPs; the core is crystalline Si and the shell is an amorphous layer composed of B, Si, and P.[44–46] The shell induces high stability in Si NPs in different environment and in different electrochemical reactions. These previous studies in combination with the small size may suggest that the B and P co-doped Si NPs exhibit high stability for charge-discharge cycles in a LIB negative electrode.

In this paper, we produce LIB negative electrodes from colloidal solutions of B and P co-doped Si NPs 2 to 12.5 nm in diameters. Since the size distribution of co-doped Si NPs in solution is relatively small, we can study the size dependence of the performance in the single-nanometer size range. We show that the negative electrode can be produced just by drop-coating the solution to a substrate and drying in air in usual atmosphere. We also show that the performance and the stability depend on the size within the small size range, and the best balance is obtained when the diameter is 7 nm.

2. EXPERIMENTAL SECTION

2.1 Preparation and characterization of B and P co-doped Si NPs.

Figure 1(a) shows the procedure to produce a methanol solution of B and P co-doped Si NPs. First, a Si-rich borophosphosilicate glass (BPSG) film was deposited on a stainless-steel plate by a cosputtering method. The sputtering target was a 4-inch-diameter sintered plate (4 mm in thickness) of phosphosilicate glass (PSG) (SiO_2 : P_2O_5 = 95:5 wt%) on which 4 pieces of crystalline Si plates (10 mm × 20 mm × 0.5 mm) and 4 pieces of B_2O_3 lumps (15 mm × 15 mm × 5 mm) were placed. Sputtering was made in an Ar gas atmosphere (2.0×10^{-2} torr) with the sputtering power of 200 W in an rf-sputtering apparatus (SPF-210HS, Anelva). The substrate was a stainless-steel plate 3 inches in diameter and 100 μm in thickness. The substrate was not intentionally heated

during the sputtering. A Si-rich BPSG film about 30 μm in thickness was deposited in 10 hours of sputtering. The thick Si-rich BPSG films were not stable on a stainless-steel plate, and cracks appeared just after the exposure to air. Therefore, the film could easily be peeled off from the plate and the flakes were collected in a crucible. The flakes were annealed in a N_2 gas atmosphere at 1000-1300 °C for 30 minutes in a tube furnace. This resulted in the disproportionation of Si-rich BPSG and the growth of B and P co-doped Si NPs in BPSG matrices. The size of Si NPs was controlled by the annealing temperature. Si NPs were then liberated from the matrices by hydrofluoric acid (HF) (48 wt.%) etching in an ultrasonic bath for 1 hour. Liberated Si NPs were transferred to methanol by using an ultrafiltration concentrator (VS0232: Sartorius Stedim Biotech GmbH).

Figure 1(b) shows a methanol solution of Si NPs just after preparation and 10 days after preparation. The solutions are very clear and no agglomerates are seen even after 10 days storage. This is a significant difference from a conventional undoped Si NPs, which quickly form agglomerates in a solution. Undoped Si NPs are also quickly oxidized in methanol when the size is in the single-nanometer range and the solution becomes whitish (see Figure S1 in Supporting Information). On the other hand, the state of Figure 2(b) continues more than years in co-doped Si NPs.

In previous work, we thoroughly characterized the B and P co-doped Si NPs by high-resolution TEM,[46] X-ray photoelectron spectroscopy (XPS),[47] Raman scattering,[47] atom probe tomography (APT),[42] etc. In Figure 1(c), we show a typical TEM image of a co-doped Si NP. We can clearly see the crystalline-core/amorphous-shell structure. The shell is not the surface oxide, since it is observed in TEM even for Si NPs just after HF etching. In these fresh Si NPs, the infrared (IR) absorption spectra are dominated by the Si-H modes and the intensity of the Si-O-Si stretching

modes is very small.[49] APT, XPS, Raman spectroscopy and IR absorption spectroscopy revealed that the amorphous shell is mainly composed of B, Si, and P, i.e., the shell is heavily B and P doped amorphous Si.[42,46,47,50] By APT, we studied the distributions of B and P in a Si NP in detail and found that B atoms preferentially stay in the outer surface and P distribution is slightly inside.[45,51] The shell is conductive and thus we can produce a thin film transistor (TFT) by using a film of codoped Si NPs as a channel.[52] The shell has the negative surface potential, which makes the NPs dispersible in methanol. The shell also provides high oxidation resistance to the NPs. This allows us to treat the NPs outside a grove box.

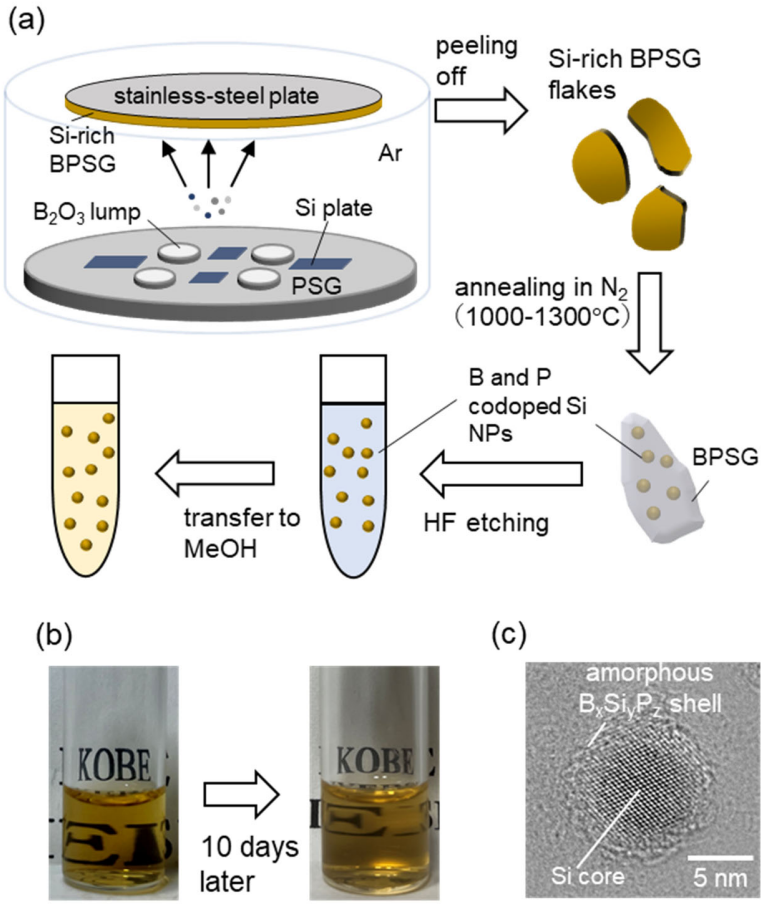


Figure 1. (a) Schematic illustration of the preparation process of B and P co-doped Si NPs. (b) Photographs of methanol solutions of Si NPs grown at 1200 °C just after preparation (left) and ten days later (right). (c) TEM image of a Si NP. The lattice fringe corresponds to {111} planes of Si crystal.

In this work, we prepare 4 different size Si NPs by changing the growth temperatures (T_a) from 1000 to 1300 °C. Figure 2(a)-(d) shows the TEM images of Si NPs grown at 1000, 1100, 1200 and 1300 °C, respectively. When the growth temperature is 1000 °C, crystalline Si NPs are scarcely observed and the irregular-shape amorphous structure is seen in the TEM image (Figure 2(a)). On the other hand, above 1100 °C, crystalline Si NPs are grown. The size increases with increasing the growth temperature. Figure 2(e) shows the size distributions obtained from the TEM images. The average diameters (D_{ave}) are 5.1, 7.0, and 12.5 nm when the growth temperature is 1100, 1200, and 1300°C, respectively. Figure. 2(f) shows Si 2p XPS spectra of Si NPs prepared with different temperatures. The spectra are measured after two days storage in methanol. Despite the very small size, the Si^0 (99.5 eV) signal can clearly be seen in addition to the signals from the oxidized states Si^{1+}- Si^{4+} (102.6-103.8 eV). The Si^0 signal is larger in higher-temperature grown Si NPs. This indicates that higher-temperature-grown Si NPs have higher oxidation resistance. It should be stressed here that in undoped Si NPs, the Si^0 signal almost disappears after storage in methanol for several days because of the formation of the native oxide with the thickness comparable to the escape depth of photoelectrons on the surface (~2 nm)[53] (see Figure S2 in Supporting Information).

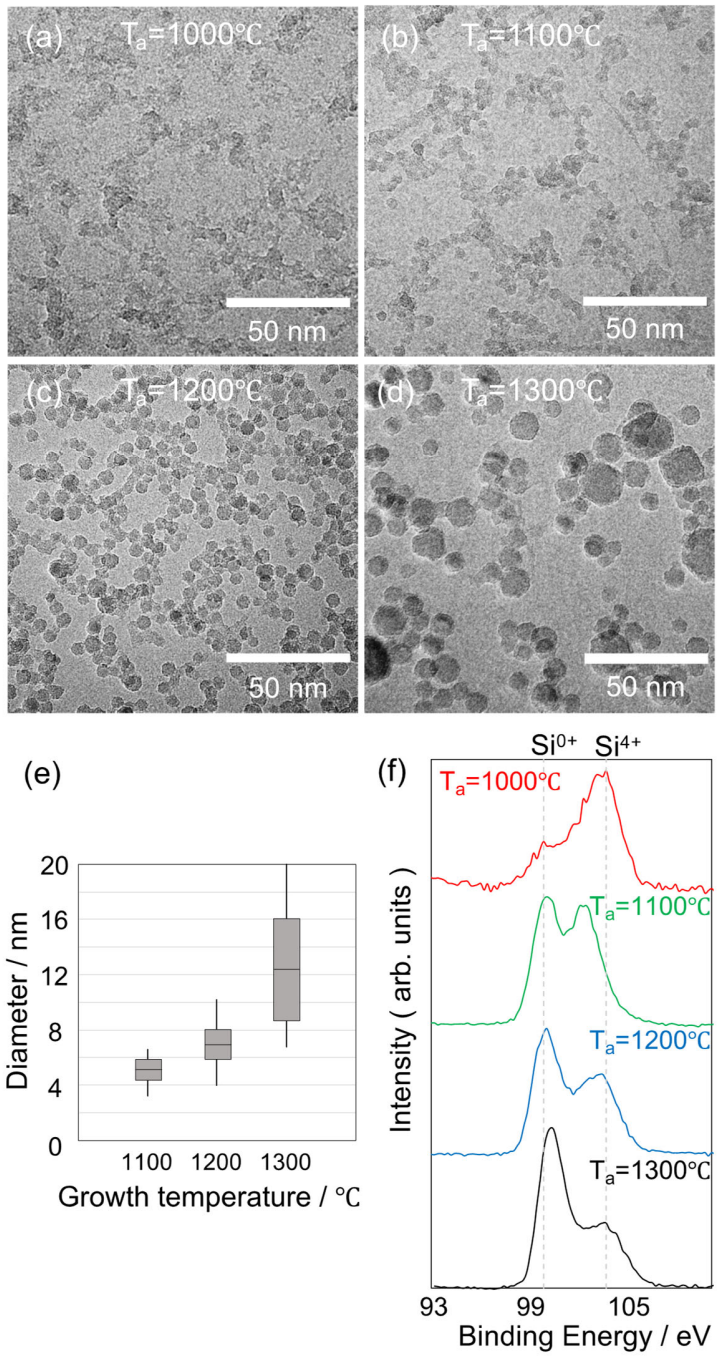


Figure 2. (a)-(d) TEM images of Si NPs grown at (a) 1000 °C, (b) 1100 °C, (c) 1200 °C, and (d) 1300 °C. (e) Diameter of Si NPs estimated from the TEM images. The gray boxes show ±σ of the size distribution and the vertical lines show the maximum and minimum diameters. The horizontal lines are the average diameters. The average diameters are 5.1, 7.0, and 12.5 nm for Si NPs grown

at 1100 °C, 1200 °C and 1300 °C, respectively. (f) Si 2p XPS spectra of Si NPs grown at different temperatures.

2.2 Preparation of electrode from methanol solution of B and P co-doped Si NPs.

In order to study intrinsic properties of B and P co-doped Si NPs as a material for a negative electrode, we do not use binders and conductive additives and employ the simplest method for the fabrication of the electrode. Figure 3(a) shows the procedure. We used a nickel (Ni) plate (0.1 mm in thickness) cut into 10 mm × 20 mm in size as a substrate. After ultraviolet-ozone surface treatment (UV-1: Samco) of a Ni plate, a methanol solution of Si NPs was dropped and dried at room temperature in atmosphere. The amount of Si NPs dropped was about 0.1 mg. The active area was 10 mm × 10 mm. Figure 3(b) shows the photograph of a Si NP electrode produced from a solution of Si NPs 7.0 nm in average diameter. Note that similar high-quality films cannot be produced from cloudy solutions of undoped Si NPs. Figure 3(c) and (d) shows the cross-sectional SEM and EDS mapping images, respectively. These images confirm the formation of a thin film of Si NPs on a Ni plate. The thickness is about 80 nm.

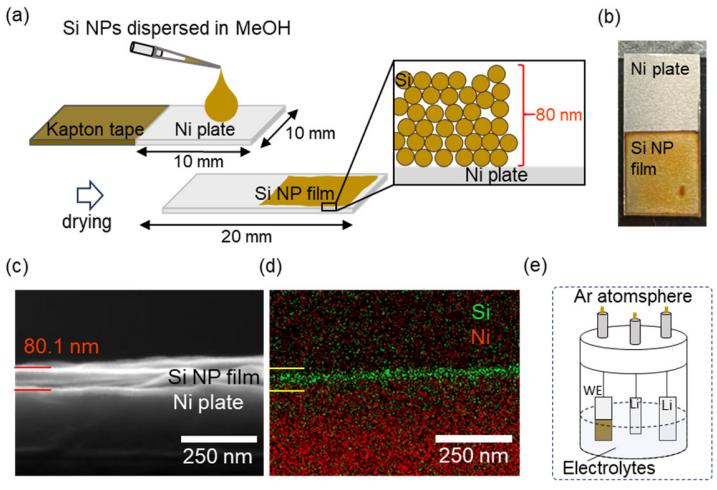


Figure 3. (a) Preparation procedure of a Si NP electrode. (b) Photograph of a Si NP electrode produced from the solution of Si NPs 7.0 nm in diameter. (c,d) Cross-sectional SEM (c) and EDS elemental mapping (d) images of a Si NP electrode. (e) Schematic of three electrodes setup for electrochemical measurement.

2.3 Electrochemical measurement

For the measurement of the charge-discharge properties, half-cells were assembled in an Ar gas atmosphere in a glove box as schematically shown in Figure 3(e). A cylindrical cell with a base diameter of 69.1 mm and a height of 96.5 mm was used for the measurements. The working electrode was a Si NP film deposited on a Ni plate, and the counter and reference electrodes were Li foils. The cell was filled with propylene carbonate (PC) (Nacalai Tesque Inc.) that was dehydrated using molecular sieve 4A (Nacalai Tesque Inc.) after dissolving lithium perchlorate ($LiClO_4$) guaranteed reagent (Kishida Chemical Co.) at concentrations of 1.0 mol L^{-1}. $LiClO_4$ was dried at 180 °C for 24 h in vacuo before dissolution. The electrochemical performance was tested in an Ar atmospheric glove box by a potentiostat (Ivium Technologies). Charge and discharge were performed at a rate of 0.2-1C within the voltage range of 0.00−2.50 V vs Li^+/Li.

3. RESULTS AND DISCUSSION

Figure 4(a)-(d) shows the cyclic voltammogram (CV) obtained for Si NP electrodes produced from different size Si NPs. In all the cases, a lithiation peak appears around 0.17 V vs Li^+/Li during the charging process, while a delithiation peak appears around 0.36 V and 0.48 V vs Li^+/Li during the discharge process. Therefore, the Si NP film produced from solutions of co-doped Si NPs work as a negative electrode. The lithiation and delithiation currents increase with Si NP size despite the

fact that the Si content is nearly the same. In the electrode made from the largest size Si NPs (12.5 nm in diameter), the lithiation and delithiation peaks gradually shift towards higher potential in each charge-discharge cycle. This suggests that the electrode is less stable compared to those made from smaller size Si NPs.

In order to see the change of Si NP structure after the lithiation/delithiation cycles, we perform Raman scattering measurements and TEM observations before and after CV measurements. Figure 4(e) shows the Raman spectrum, the TEM image and the FFT image of the electrode made from 7.0 nm Si NPs before the CV measurement. The TEM image is obtained by scraping off a small amount of NPs from the electrode surface. The Raman spectrum has crystalline Si peak at 520 cm^{-1}. This is consistent with the lattice fringes in the TEM image and the spots in the FFT image corresponding to the {111} planes of Si crystal. The broad Raman band around 620 cm^{-1} arises from B-related local vibrations from the amorphous shell. In the case of undoped Si NPs, no such peak exists (see Figure S3 in Supporting Information). Figure 4(f) and (g) shows the Raman spectra, the TEM images and the FFT images after 2 and 10 cycles, respectively. We can see the decrease of the intensity of the crystalline peak by the CV measurements. After 10 cycles, the peak disappears and only a broad band around 480 cm^{-1} remains. This is the signature of the amorphization and is consistent with the disappearance of the spots in the FFT images. The amorphization by the lithiation/delithiation cycles provides the evidence that the single-nanometer-size B and P co-doped Si NPs work as the active material for a negative electrode. In the Raman spectrum in Figure 4(g), a broad band around 620 cm^{-1} remains even after 10 cycles. This may suggest that the amorphous shell is very stable for the lithiation/delithiation processes.

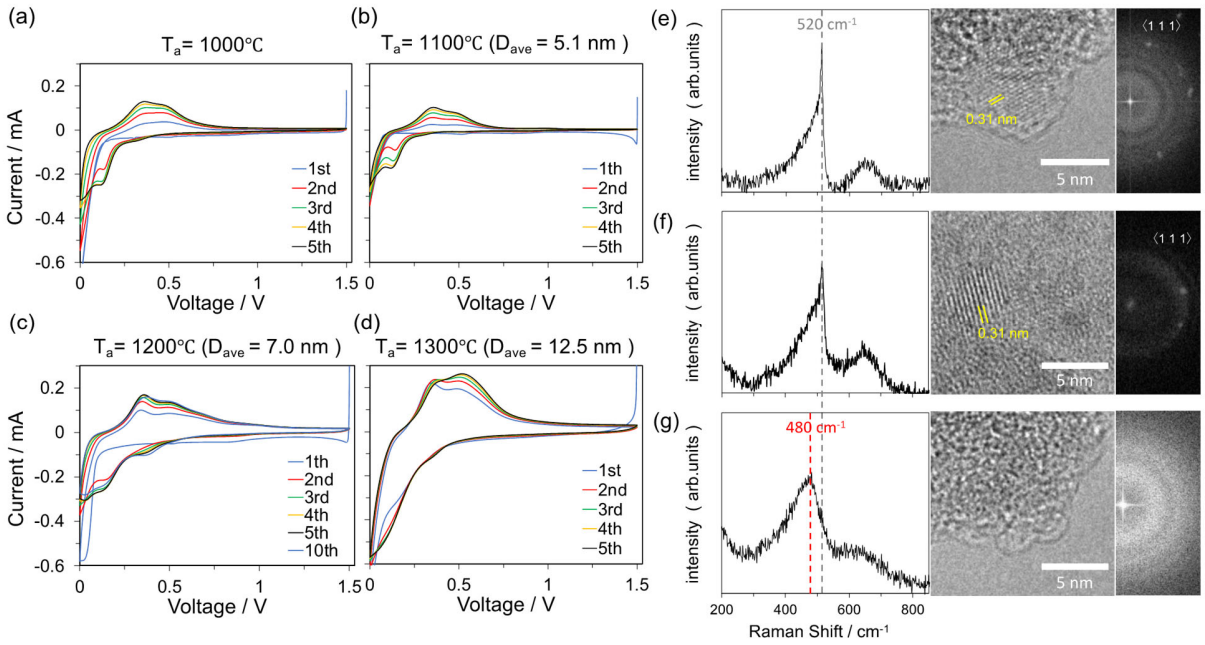


Figure 4. (a)-(d) CV curves of electrodes made from Si NPs grown at different temperatures, (a) 1000 °C, (b) 1100 °C (D_{ave}=5.1 nm), (c) 1200 °C (D_{ave}=7.0 nm) and (d) 1300 °C (D_{ave}=12.5 nm). (e)-(g) Raman scattering spectra, TEM images and the corresponding FFT images of a Si NP electrode produced from Si NPs 7.0 nm in average diameter before CV measurement (e) and after 2 cycles (f) and 10 (g) cycles.

Figure 5(a-d) shows the charge-discharge potential profiles (0.0 - 2.5 V vs Li^+/Li) at 0.5C-rate obtained for Si NP electrodes produced from different size Si NPs, and Figure 5(e) shows the discharge capacity up to 30 cycles. The capacity is in between the theoretical value of carbon (372 mAh/g) and that of Si (4200 mAh/g). The capacity depends strongly on the size of Si NPs. In Si NPs grown at the lowest temperatures (1000 °C), the initial capacity is relatively low. This is due to the higher proportion of surface oxide with respect to the total volume as can be seen in the XPS spectrum in Figure 2(f). The initial capacity increases with the Si NP size, reaches the maximum when the diameter is 7.0 nm, and then slightly decreases.

In Figure 5(e), the capacity gradually increases with the cycle in smaller size Si NPs, while it decreases in larger size Si NPs. In the electrode made from Si NPs grown at the lowest temperatures (1000 °C), the capacity retention, i.e., the ratio of the capacity between the initial and after 30th cycles, reaches 127 %. It decreases with increasing the size and is 58 % in the largest size Si NPs (D_{ave}=12.5 nm). The capacity decrease suggests destruction of the electrodes during the cycles and continuous formation of SEI. This is consistent with the shift of the lithiation and delithiation peaks towards higher potential in the CV cycles in Figure 4(d). These results suggest that, even in the single nanometer-size range, size reduction plays a positive role to prevent the structural breakdown, although the initial capacitance decreases due to the decrease of the volume of non-surface Si.

Figure 5(f) shows the coulombic efficiency up to 30 cycles. The initial coulombic efficiency of small Si NPs, i.e., those grown at 1000 °C and 1100 °C, at the early cycles is smaller than others, and it gradually increases with the cycle. This phenomenon may be related to the XPS data in Figure 2(f). Figure 2(f) indicates that lower-temperature-grown Si NPs are more vulnerable for oxidation, and thus they are expected to have lower conductivity compared to higher temperature grown ones. The low conductivity results in the slow formation of SEI and gradual increase of the coulombic efficiency. In Figure 5(f), the coulombic efficiency is the most stable in 7.0 nm-diameter Si NPs and the highest value is 97.8 %. Combining the data in Figure 4 and 5, Si NPs 7.0 nm in diameter has the highest performance among different size B and P co-doped Si NPs. Figure 5(g) shows charge-discharge potential profiles of the electrode of Si NPs 7.0 nm in diameter measured at various current densities, and Figure 5(h) shows the discharge capacity up to 30 cycles. The capacity reaches around 3300 mAh/g at 0.2C-rate.

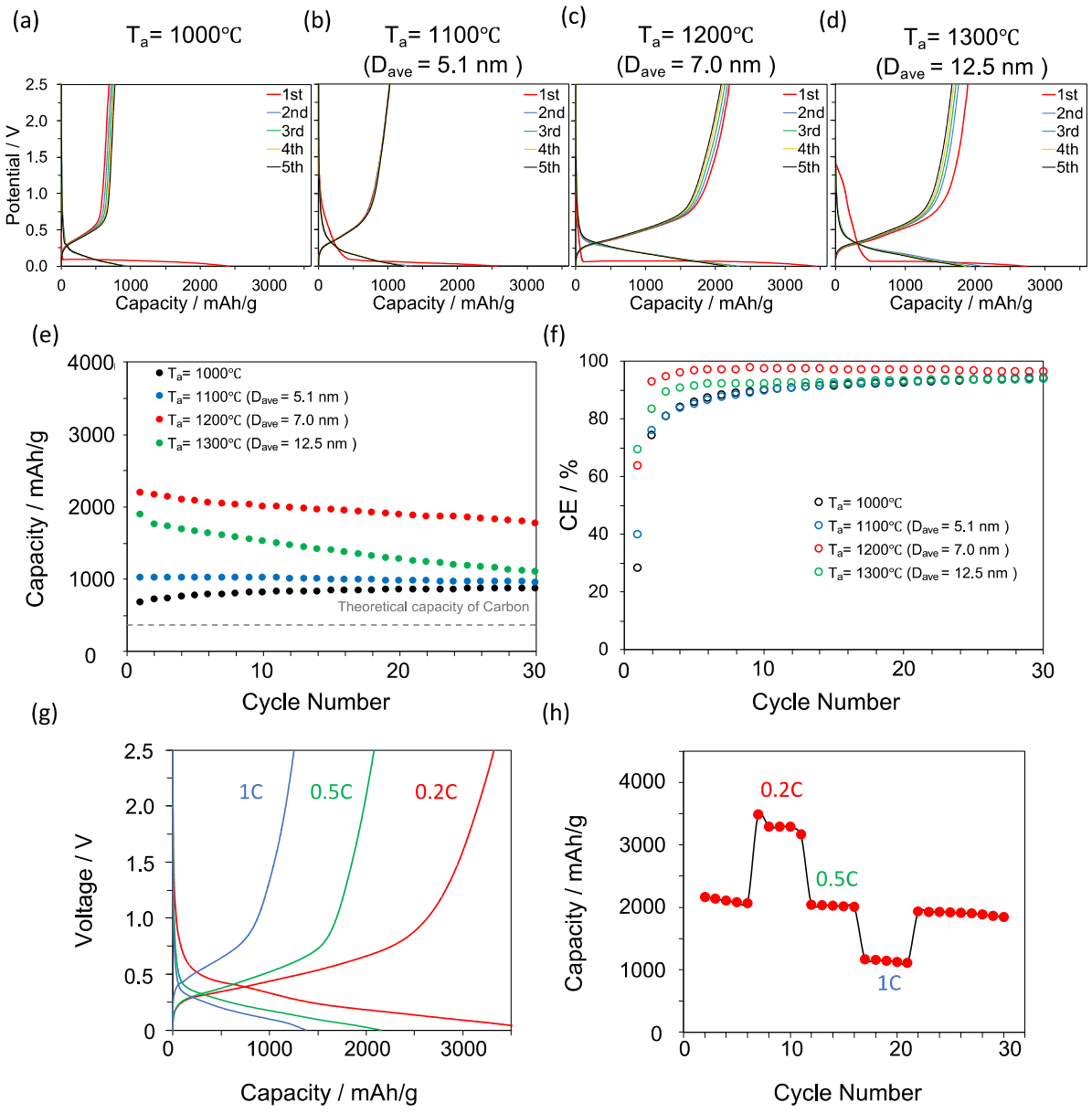


Figure5. (a-d) Charge-discharge potential profiles (0.0 - 2.5 V vs Li^+/Li) at 0.5 C-rate (1C-rate = 4.2 Ag^{-1}) of electrodes made from Si NPs grown at different temperatures, (a) 1000 °C, (b) 1100 °C (D_{ave}=5.1 nm), (c) 1200 °C (D_{ave}=7.0 nm), and (d) 1300 °C (D_{ave}=12.5 nm). (e) Discharge capacity up to 30 cycles. (f) coulombic efficiency at 0.5C-rate. (g, h) Charge-discharge potential

profiles measured at various C-rate (g) and discharge capacity up to 30 cycles (h) of the electrode made from Si NPs 7.0 nm in diameter.

4. CONCLUSION

We produced a Si NP electrode for LiB from methanol solutions of single-nanometer-size B and P co-doped Si NPs by drop-coating the solution on a substrate in air, and studied the size dependence of the performance and the stability. The diameter of Si NPs was changed from less than 2 nm to 12.5 nm. We showed that all the films produced from different size Si NPs worked as a negative electrode without binders and conductive additives, and they did not peel off during 30 charge-discharge cycles. We also showed that the performance and the stability depend strongly on the size. The initial capacity increased with the size, while the stability decreased. We found that the optimum diameter is ~7 nm. In the electrode made from 7.0 nm-diameter Si NPs, the capacity was ~3300 mAh/g and the Coulombic efficiency was ~97 % at 0.2C-rate.

Supporting Information

Photos of MeOH solutions of undoped Si NPs immediately after preparation and after three days, Si 2p XPS spectrum of undoped Si NPs grown at 1200 °C, and Raman scattering spectrum of undoped Si NPs grown at 1200 °C before a charge/discharge measurement.

Acknowledgement

This work is partially supported by JSPS KAKENHI, Grant Numbers 18KK0141.

References

(1) Li, M.; Lu, J.; Chen, Z.; Amine, K. 30 Years of Lithium-Ion Batteries. *Adv. Mater.* **2018**, *30* (33), 1800561, 1–24. https://doi.org/10.1002/adma.201800561.

(2) Armand, M.; Tarascon, J.-M. Building Better Batteries. *Nature* **2008**, *451* (7179), 652–657. https://doi.org/10.1038/451652a.

(3) Blomgren, G. E. The Development and Future of Lithium Ion Batteries. *J. Electrochem. Soc.* **2017**, *164* (1), A5019–A5025. https://doi.org/10.1149/2.0251701jes.

(4) Manthiram, A. An Outlook on Lithium Ion Battery Technology. *ACS Cent. Sci.* **2017**, *3* (10), 1063–1069. https://doi.org/10.1021/acscentsci.7b00288.

(5) Manthiram, A. Materials Challenges and Opportunities of Lithium Ion Batteries. *J. Phys. Chem. Lett.* **2011**, *2* (3), 176–184. https://doi.org/10.1021/jz1015422.

(6) Huang, X.; Zeng, Z.; Fan, Z.; Liu, J.; Zhang, H. Graphene-Based Electrodes. *Adv. Mater.* **2012**, *24* (45), 5979–6004. https://doi.org/10.1002/adma.201201587.

(7) Zhu, J.; Yang, D.; Yin, Z.; Yan, Q.; Zhang, H. Graphene and Graphene-Based Materials for Energy Storage Applications. *Small* **2014**, *10* (17), 3480–3498. https://doi.org/10.1002/smll.201303202.

(8) Raccichini, R.; Varzi, A.; Passerini, S.; Scrosati, B. The Role of Graphene for Electrochemical Energy Storage. *Nat. Mater.* **2015**, *14* (3), 271–279. https://doi.org/10.1038/nmat4170.

(9) Goriparti, S.; Miele, E.; De Angelis, F.; Di Fabrizio, E.; Proietti Zaccaria, R.; Capiglia, C. Review on Recent Progress of Nanostructured Anode Materials for Li-Ion Batteries. *J. Power Sources* **2014**, *257*, 421–443. https://doi.org/10.1016/j.jpowsour.2013.11.103.

(10) Li, H.; Wang, Z.; Chen, L.; Huang, X. Research on Advanced Materials for Li-Ion Batteries. *Adv. Mater.* **2009**, *21* (45), 4593–4607. https://doi.org/10.1002/adma.200901710.

(11) Ma, D.; Cao, Z.; Hu, A. Si-Based Anode Materials for Li-Ion Batteries: A Mini Review. *Nano-Micro Lett.* **2014**, *6* (4), 347–358. https://doi.org/10.1007/s40820-014-0008-2.

(12) Wu, H.; Cui, Y. Designing Nanostructured Si Anodes for High Energy Lithium Ion Batteries. *Nano Today* **2012**, *7* (5), 414–429. https://doi.org/10.1016/j.nantod.2012.08.004.

(13) Radvanyi, E.; Porcher, W.; De Vito, E.; Montani, A.; Franger, S.; Jouanneau Si Larbi, S. Failure Mechanisms of Nano-Silicon Anodes upon Cycling: An Electrode Porosity Evolution Model. *Phys. Chem. Chem. Phys.* **2014**, *16* (32), 17142–17153. https://doi.org/10.1039/C4CP02324B.

(14) Bashir, S.; Hanumandla, P.; Huang, H.-Y.; Liu, J. L. Nanostructured Materials for Advanced Energy Conversion and Storage Devices: Safety Implications at End-of-Life Disposal. *Nanostructured Mater. Next-Generation Energy Storage Convers.* **2018**, *4*, 517–542. https://doi.org/10.1007/978-3-662-56364-9_18.

(15) Kasavajjula, U.; Wang, C.; Appleby, A. J. Nano- and Bulk-Silicon-Based Insertion Anodes for Lithium-Ion Secondary Cells. *J. Power Sources* **2007**, *163* (2), 1003–1039. https://doi.org/10.1016/j.jpowsour.2006.09.084.

(16) An, Y.; Fei, H.; Zeng, G.; Ci, L.; Xiong, S.; Feng, J.; Qian, Y. Green, Scalable, and Controllable Fabrication of Nanoporous Silicon from Commercial Alloy Precursors for

High-Energy Lithium-Ion Batteries. *ACS Nano* **2018**, *12* (5), 4993–5002. https://doi.org/10.1021/acsnano.8b02219.

(17) Huang, G.; Han, J.; Lu, Z.; Wei, D.; Kashani, H.; Watanabe, K.; Chen, M. Ultrastable Silicon Anode by Three-Dimensional Nanoarchitecture Design. *ACS Nano* **2020**, *14* (4), 4374–4382. https://doi.org/10.1021/acsnano.9b09928.

(18) Wada, T.; Ichitsubo, T.; Yubuta, K.; Segawa, H.; Yoshida, H.; Kato, H. Bulk-Nanoporous-Silicon Negative Electrode with Extremely High Cyclability for Lithium-Ion Batteries Prepared Using a Top-Down Process. *Nano Lett.* **2014**, *14* (8), 4505–4510. https://doi.org/10.1021/nl501500g.

(19) Chan, C. K.; Peng, H.; Liu, G.; McIlwrath, K.; Zhang, X. F.; Huggins, R. A.; Cui, Y. High-Performance Lithium Battery Anodes Using Silicon Nanowires. *Nat. Nanotechnol.* **2008**, *3* (1), 31–35. https://doi.org/10.1038/nnano.2007.411.

(20) Park, M.-H.; Kim, M. G.; Joo, J.; Kim, K.; Kim, J.; Ahn, S.; Cui, Y.; Cho, J. Silicon Nanotube Battery Anodes. *Nano Lett.* **2009**, *9* (11), 3844–3847. https://doi.org/10.1021/nl902058c.

(21) Yu, W.-J.; Liu, C.; Hou, P.-X.; Zhang, L.; Shan, X.-Y.; Li, F.; Cheng, H.-M. Lithiation of Silicon Nanoparticles Confined in Carbon Nanotubes. *ACS Nano* **2015**, *9* (5), 5063–5071. https://doi.org/10.1021/acsnano.5b00157.

(22) Wu, M.; Sabisch, J. E. C.; Song, X.; Minor, A. M.; Battaglia, V. S.; Liu, G. In Situ Formed Si Nanoparticle Network with Micron-Sized Si Particles for Lithium-Ion Battery Anodes. *Nano Lett.* **2013**, *13* (11), 5397–5402. https://doi.org/10.1021/nl402953h.

(23) Liu, X. H.; Zhong, L.; Huang, S.; Mao, S. X.; Zhu, T.; Huang, J. Y. Size-Dependent Fracture of Silicon Nanoparticles During Lithiation. *ACS Nano* **2012**, *6* (2), 1522–1531. https://doi.org/10.1021/nn204476h.

(24) Hwang, T. H.; Lee, Y. M.; Kong, B.-S.; Seo, J.-S.; Choi, J. W. Electrospun Core–Shell Fibers for Robust Silicon Nanoparticle-Based Lithium Ion Battery Anodes. *Nano Lett.* **2012**, *12* (2), 802–807. https://doi.org/10.1021/nl203817r.

(25) Kim, H.; Seo, M.; Park, M.-H.; Cho, J. A Critical Size of Silicon Nano-Anodes for Lithium Rechargeable Batteries. *Angew. Chemie Int. Ed.* **2010**, *49* (12), 2146–2149. https://doi.org/10.1002/anie.200906287.

(26) Ge, M.; Rong, J.; Fang, X.; Zhang, A.; Lu, Y.; Zhou, C. Scalable Preparation of Porous Silicon Nanoparticles and Their Application for Lithium-Ion Battery Anodes. *Nano Res.* **2013**, *6* (3), 174–181. https://doi.org/10.1007/s12274-013-0293-y.

(27) Li, P.; Hwang, J.-Y.; Sun, Y.-K. Nano/Microstructured Silicon–Graphite Composite Anode for High-Energy-Density Li-Ion Battery. *ACS Nano* **2019**, *13* (2), acsnano.9b00169. https://doi.org/10.1021/acsnano.9b00169.

(28) Ren, Y.; Zhou, X.; Tang, J.; Ding, J.; Chen, S.; Zhang, J.; Hu, T.; Yang, X.-S.; Wang, X.; Yang, J. Boron-Doped Spherical Hollow-Porous Silicon Local Lattice Expansion toward a High-Performance Lithium-Ion-Battery Anode. *Inorg. Chem.* **2019**, *58* (7), 4592–4599. https://doi.org/10.1021/acs.inorgchem.9b00158.

(29) Gordon, I. P.; Xu, W.; Randak, S.; Jow, T. R.; Stadie, N. P. Stabilizing Effects of Phosphorus-Doped Silicon Nanoparticle Anodes in Lithium-Ion Batteries. *Chem. Mater.* **2023**, *35* (2), 549–557. https://doi.org/10.1021/acs.chemmater.2c02983.

(30) Liu, X. H.; Zhang, L. Q.; Zhong, L.; Liu, Y.; Zheng, H.; Wang, J. W.; Cho, J.-H.; Dayeh, S. A.; Picraux, S. T.; Sullivan, J. P.; Mao, S. X.; Ye, Z. Z.; Huang, J. Y. Ultrafast Electrochemical Lithiation of Individual Si Nanowire Anodes. *Nano Lett.* **2011**, *11* (6), 2251–2258. https://doi.org/10.1021/nl200412p.

(31) Huang, S.; Cheong, L.-Z.; Wang, D.; Shen, C. Nanostructured Phosphorus Doped Silicon/Graphite Composite as Anode for High-Performance Lithium-Ion Batteries. *ACS Appl. Mater. Interfaces* **2017**, *9* (28), 23672–23678. https://doi.org/10.1021/acsami.7b04361.

(32) Domi, Y.; Usui, H.; Shimizu, M.; Kakimoto, Y.; Sakaguchi, H. Effect of Phosphorus-Doping on Electrochemical Performance of Silicon Negative Electrodes in Lithium-Ion Batteries. *ACS Appl. Mater. Interfaces* **2016**, *8* (11), 7125–7132. https://doi.org/10.1021/acsami.6b00386.

(33) Tang, F.; Tan, Y.; Jiang, T.; Zhou, Y. Phosphorus-Doped Silicon Nanoparticles as High Performance LIB Negative Electrode. *J. Mater. Sci.* **2022**, *57* (4), 2803–2812. https://doi.org/10.1007/s10853-021-06679-3.

(34) Qu, X.; Zhang, X.; Wu, Y.; Hu, J.; Gao, M.; Pan, H.; Liu, Y. An Eggshell-Structured N-Doped Silicon Composite Anode with High Anti-Pulverization and Favorable Electronic Conductivity. *J. Power Sources* **2019**, *443*, 227265, 1–10. https://doi.org/10.1016/j.jpowsour.2019.227265.

(35) Zhao, L.; Bennett, J. C.; George, A.; Obrovac, M. N. SiC-Free Carbon–Silicon Alloys Prepared by Delithiation as Lithium-Ion Battery Negative Electrodes. *Chem. Mater.* **2019**, *31* (11), 3883–3890. https://doi.org/10.1021/acs.chemmater.8b03898.

(36) Yang, Y.; Liu, S.; Bian, X.; Feng, J.; An, Y.; Yuan, C. Morphology- and Porosity-Tunable Synthesis of 3D Nanoporous SiGe Alloy as a High-Performance Lithium-Ion Battery Anode. *ACS Nano* **2018**, *12* (3), 2900–2908. https://doi.org/10.1021/acsnano.8b00426.

(37) Kim, H.; Son, Y.; Park, C.; Lee, M.-J.; Hong, M.; Kim, J.; Lee, M.; Cho, J.; Choi, H. C. Germanium Silicon Alloy Anode Material Capable of Tunable Overpotential by Nanoscale Si Segregation. *Nano Lett.* **2015**, *15* (6), 4135–4142. https://doi.org/10.1021/acs.nanolett.5b01257.

(38) Fujii, M.; Sugimoto, H.; Imakita, K. All-Inorganic Colloidal Silicon Nanocrystals—Surface Modification by Boron and Phosphorus Co-Doping. *Nanotechnology* **2016**, *27* (26), 262001, 1–20. https://doi.org/10.1088/0957-4484/27/26/262001.

(39) Fujii, M.; Sugimoto, H.; Kano, S. Colloidal Solution of Boron and Phosphorus Codoped Silicon Quantum Dots—from Material Development to Applications. *Jpn. J. Appl. Phys.* **2022**, *61*, SA0807, 1–12. https://doi.org/10.35848/1347-4065/ac1c3f.

(40) Fujii, M.; Sugimoto, H.; Kano, S. Silicon Quantum Dots with Heavily Boron and Phosphorus Codoped Shell. *Chem. Commun.* **2018**, *54* (35), 4375–4389. https://doi.org/10.1039/C8CC01612G.

(41) Sugimoto, H.; Yamamura, M.; Fujii, R.; Fujii, M. Donor–Acceptor Pair Recombination in Size-Purified Silicon Quantum Dots. *Nano Lett.* **2018**, *18* (11), 7282–7288. https://doi.org/10.1021/acs.nanolett.8b03489.

(42) Sugimoto, H.; Zhou, H.; Takada, M.; Fushimi, J.; Fujii, M. Visible-Light Driven Photocatalytic Hydrogen Generation by Water-Soluble All-Inorganic Core–Shell Silicon Quantum Dots. *J. Mater. Chem. A* **2020**, *8* (31), 15789–15794. https://doi.org/10.1039/D0TA01071E.

(43) Takada, M.; Inoue, K.; Sugimoto, H.; Fujii, M. Solution-Processed Silicon Quantum Dot Photocathode for Hydrogen Evolution. *Nanotechnology* **2021**, *32* (48), 485709, 1–7. https://doi.org/10.1088/1361-6528/ac09e0.

(44) Sugimoto, H.; Fujii, M.; Imakita, K.; Hayashi, S.; Akamatsu, K. All-Inorganic Near-Infrared Luminescent Colloidal Silicon Nanocrystals: High Dispersibility in Polar Liquid by Phosphorus and Boron Codoping. *J. Phys. Chem. C* **2012**, *116* (33), 17969–17974. https://doi.org/10.1021/jp305832x.

(45) Nomoto, K.; Sugimoto, H.; Breen, A.; Ceguerra, A. V.; Kanno, T.; Ringer, S. P.; Wurfl, I. P.; Conibeer, G.; Fujii, M. Atom Probe Tomography Analysis of Boron and/or Phosphorus Distribution in Doped Silicon Nanocrystals. *J. Phys. Chem. C* **2016**, *120* (31), 17845–17852. https://doi.org/10.1021/acs.jpcc.6b06197.

(46) Sugimoto, H.; Yamamura, M.; Sakiyama, M.; Fujii, M. Visualizing a Core–Shell Structure of Heavily Doped Silicon Quantum Dots by Electron Microscopy Using an Atomically Thin Support Film. *Nanoscale* **2018**, *10* (16), 7357–7362. https://doi.org/10.1039/C7NR09474D.

(47) Fujii, M.; Sugimoto, H.; Hasegawa, M.; Imakita, K. Silicon Nanocrystals with High Boron and Phosphorus Concentration Hydrophilic Shell—Raman Scattering and X-Ray Photoelectron Spectroscopic Studies. *J. Appl. Phys.* **2014**, *115* (8), 084301. https://doi.org/10.1063/1.4866497.

(48) Nomoto, K.; Sugimoto, H.; Ceguerra, A. V.; Fujii, M.; Ringer, S. P. 3D Microstructure Analysis of Silicon–Boron Phosphide Mixed Nanocrystals. *Nanoscale* **2020**, *12* (13), 7256–7262. https://doi.org/10.1039/D0NR01023E.

(49) Ashkenazi, O.; Azulay, D.; Balberg, I.; Kano, S.; Sugimoto, H.; Fujii, M.; Millo, O. Size-Dependent Donor and Acceptor States in Codoped Si Nanocrystals Studied by Scanning Tunneling Spectroscopy. *Nanoscale* **2017**, *9* (45), 17884–17892. https://doi.org/10.1039/c7nr06257e.

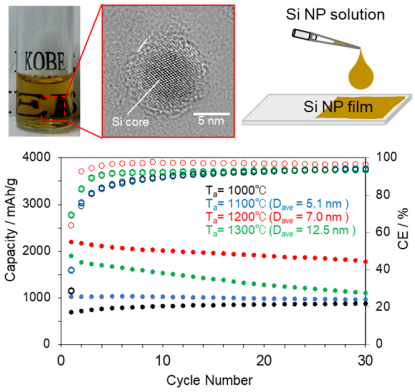
(50) Minami, A.; Sugimoto, H.; Crowe, I. F.; Fujii, M. Growth of Core–Shell Silicon Quantum Dots in Borophosphosilicate Glass Matrix: Raman and Transmission Electron Microscopic Studies. *J. Phys. Chem. C* **2018**, *122* (36), 21069–21075. https://doi.org/10.1021/acs.jpcc.8b07316.

(51) Nomoto, K.; Sugimoto, H.; Cui, X. Y.; Ceguerra, A. V.; Fujii, M.; Ringer, S. P. Distribution of Boron and Phosphorus and Roles of Co-Doping in Colloidal Silicon Nanocrystals. *Acta Mater.* **2019**, *178*, 186–193. https://doi.org/10.1016/j.actamat.2019.08.013.

(52) Kano, S.; Tada, Y.; Matsuda, S.; Fujii, M. Solution Processing of Hydrogen-Terminated Silicon Nanocrystal for Flexible Electronic Device. *ACS Appl. Mater. Interfaces* **2018**, *10* (24), 20672–20678. https://doi.org/10.1021/acsami.8b04072.

(53) Lu, Z. H.; McCaffrey, J. P.; Brar, B.; Wilk, G. D.; Wallace, R. M.; Feldman, L. C.; Tay, S. P. SiO 2 Film Thickness Metrology by X-Ray Photoelectron Spectroscopy. *Appl. Phys. Lett.* **1997**, *71* (19), 2764–2766. https://doi.org/10.1063/1.120438.

TOC graphic


KOBE
Si core
5 nm
Si NP solution
Si NP film
Capacity / mAh/g
CE / %
Cycle Number
T_a= 1000℃
T_a= 1100℃ (D_{ave} = 5.1 nm)
T_a= 1200℃ (D_{ave} = 7.0 nm)
T_a= 1300℃ (D_{ave} = 12.5 nm)